AGU PUBLICATIONS

Geochemistry, Geophysics, Geosystems

RESEARCH ARTICLE

10.1002/2013GC005186

Key Points:
- V_P/V_s is more difficult to relate to composition then previously thought
- I introduce a new anisotropic H-κ stacking technique
- Melt beneath the Afar Depression is stored in interconnected lower crustal sills

Supporting Information:
- ReadMe
- Tables S1–S2

Correspondence to:
J. O. S. Hammond,
j.hammond@imperial.ac.uk

Citation:
Hammond, J. O. S. (2014), Constraining melt geometries beneath the Afar Depression, Ethiopia from teleseismic receiver functions: The anisotropic H-κ stacking technique, *Geochem. Geophys. Geosyst.*, *15*, 1316–1332, doi:10.1002/2013GC005186.

Received 4 DEC 2013
Accepted 8 FEB 2014
Accepted article online 12 MAR 2014
Published online 25 APR 2014

Constraining melt geometries beneath the Afar Depression, Ethiopia from teleseismic receiver functions: The anisotropic H-κ stacking technique

J. O. S. Hammond[1]

[1]Imperial College London, South Kensington Campus, London, UK

Abstract Understanding the nature of the crust has long been a goal for seismologists when imaging the Earth. This is particularly true in volcanic regions where imaging melt storage and migration can have important implications for the size and nature of an eruption. Receiver functions and the H-κ stacking (Hκ) technique are often used to constrain crustal thickness (H) and the ratio of *P* to *S* wave velocities (κ). In this paper, I show that it is essential to consider anisotropy when performing Hκ. I show that in a medium with horizontally transverse isotropy a strong variation in κ with back azimuth is present, which characterizes the anisotropic medium. In a vertically transverse isotropic medium, no variation in κ with back azimuth is observed, but κ is increased across all back azimuths. Thus, estimates of κ are more difficult to relate to composition than previously thought. I extend these models to melt-induced anisotropy and show that similar patterns are observed, but with more significant variations and increases in κ. Based on these observations, I develop a new anisotropic H-κ stacking technique which inverts Hκ data for melt fraction, aspect ratio, and orientation of melt inclusions. I apply this to data for the Afar Depression and show that melt is stored in interconnected stacked sills in the lower crust, which likely supply the recent volcanic eruptions and dike intrusions. This new technique can be applied to any anisotropic medium where it can provide constraints on the average crustal anisotropy.

1. Introduction

In volcanically active regions, understanding how melt is stored, for example, in dikes or sills, and how it migrates can have important implications for the nature and style of volcanic eruption [*Blundy and Cashman*, 2008]. Seismology has often been used to provide snapshots of the crust in an attempt to determine its structure and composition [e.g., *Mooney and Brocher*, 1987; *Zandt and Ammon*, 1995; *Kind et al*., 1996; *Laske et al*., 2013], but questions about melt storage remain the subject of debate. Large trade-offs exist in the role melt fraction and melt geometry play on the velocity reduction [*Blackman and Kendall*, 1997], which means the details of melt amounts and storage are poorly constrained.

Recently, receiver functions, a technique which uses converted *P* wave energy to *S* wave energy from teleseismic earthquakes, has become a common method to image the bulk crustal structure beneath a seismic array. This technique provides important constraints on the crustal thickness, internal structure, and crustal composition at the fraction of the cost than large controlled source experiments with the added advantage of providing a larger spatial coverage. A common processing technique used on receiver function data is H-κ stacking [*Zandt and Ammon*, 1995; *Zhu and Kanamori*, 2000], a method that uses the trade-off between the crustal thickness (*H*) and the ratio of *P* wave to *S* wave velocities (V_P/V_S; κ) to place constraints on both these parameters (Figure 1). This has provided insights into the formation of continental crust [e.g., *Zandt and Ammon*, 1995; *Gupta*, 2003], the tectonic deformation beneath a region [e.g., *Mohsen et al*., 2005], and the presence of melt in volcanic regions [*Dugda et al*., 2005; *Stuart et al*., 2006; *Hammond et al*., 2011]. However, to date, all these studies have been performed assuming an isotropic crust. Variation in seismic velocity due to anisotropy (the variation of seismic wave speed with direction of propagation) can affect the arrival times and amplitudes of the converted phases [*Levin and Park*, 1997a, 1997b; *Savage*, 1998; *Liu and Niu*, 2012] and so may have a large effect on the H-κ stacking technique. In this paper, I investigate the effect of anisotropy on the H-κ stacking technique and show that the resulting estimates of H and κ are in fact apparent measurements and are more difficult to relate to composition than previously thought. I use this observation to show how melt alignment beneath the Ethiopian Afar Depression gives rise to high apparent V_P/V_S

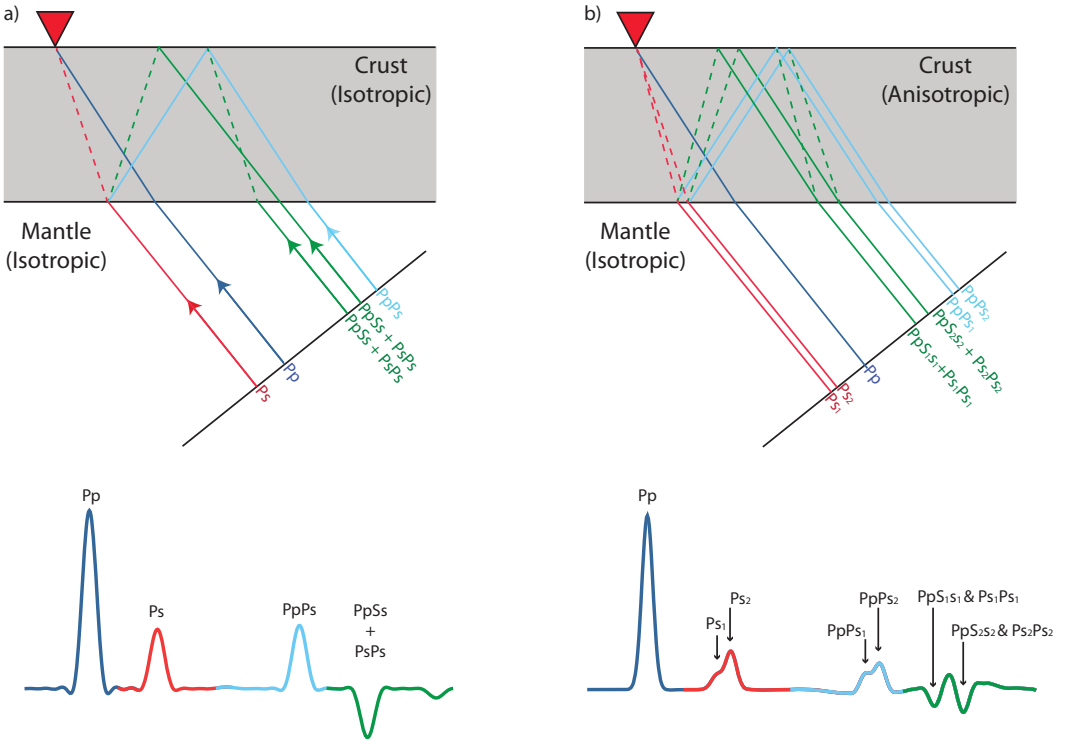

Figure 1. Cartoon showing (a) receiver function generated for a simple isotropic crust over a half-space and (b) receiver functions generated for a crust with HTI anisotropy over a half-space. Top plots show the simple crustal model where solid lines show *P* wave paths and dashed lines show *S* wave paths. Bottom plots show the receiver function traces where colors relate to the different phases in the top plot. Note the complicated receiver function for the anisotropic crust due to the split shear waves.

and the variation in apparent V_P/V_S with back azimuth can place important constraints on the geometry of melt storage in the crust.

2. Receiver Functions and the H-κ Stacking Technique

Receiver functions are a common technique to image bulk crustal structure beneath an array of seismic stations. The technique takes advantage of the fact that buried in the *P* wave coda are many *P* to *S* wave conversions (*Ps*) from discontinuities directly beneath a seismic station [*Langston*, 1979]. It is possible to isolate these conversions by deconvolving the *P* wave signal from the horizontal components, either in the frequency domain [*Langston*, 1979; *Owens et al.*, 1984; *Ammon*, 1991; *Park and Levin*, 2000; *Helffrich*, 2006], or time domain [*Oldenburg*, 1981; *Abers et al.*, 1995; *Gurrola et al.*, 1995; *Ligorria and Ammon*, 1999]. This removes the source and far-field effects, leaving the receiver function which contains primarily the *Ps* arrivals (Figure 1).

Typically, the dominant signal in the first few seconds of the receiver function is the *Ps* conversion from the Moho, followed by reverberated phases within the crust (Figure 1). A common second step in the data analysis is to use the *Ps* conversion from the Moho and the multiples to try and understand the crustal thickness and bulk crustal V_P/V_S beneath a seismic array. This is called the *H*-κ stacking technique (herein referred to as Hκ) [*Zandt and Ammon*, 1995; *Zhu and Kanamori*, 2000]. The power of this technique comes from the fact that the arrival times of the *Ps* arrival and the reverberated phases (*PpPs*, *PpSs*, and *PsPs*) depend on the thickness of the crust (*H*), the ratio of *P* to *S* wave velocities (assuming some knowledge of the average *P* or *S* wave velocities in the crust) and the slowness of the incoming seismic energy (*p*; see *Zhu and Kanamori* [2000] for more details). Due to the simplicity of this method, it has become one of the standard techniques in the seismologists toolbox.

3. Anisotropic H-κ Stacking

Many studies have shown that the presence of anisotropy can affect the amplitude and arrival times of the *Ps* conversions on both the radial and transverse components (Figure 1) [e.g., *Levin and Park*, 1997a, 1997b;

Table 1. List of Parameters Searched in the Grid Search Inversion

Parameter	Range Searched	Increment
Horizontal inclusions aspect ratio	0.00–1.00	0.01 (0.00–0.10)
		0.02 (0.12–0.20)
		0.05 (0.25–0.50)
		0.10 (0.60–1.00)
Horizontal melt fraction	0–16%	1%
Vertical inclusions aspect ratio	0.00–1.00	0.01 (0.00–0.10)
		0.02 (0.12–0.20)
		0.05 (0.25–0.50)
		0.10 (0.60–1.00)
Vertical melt fraction	0–16%	1%
Vertical melt inclusion orientation	10–180°	10°
	10–180°	10°

Savage, 1998; *Liu and Niu*, 2012]. This occurs because a *P* to *S* wave conversion at the base of an anisotropic medium generates two shear waves, one traveling in the fast shear wave orientation, the other perpendicular to this. The presence of energy on the transverse component and variations in the *Ps* arrival time with back azimuth on the radial and transverse component, both with $cos2\theta$ variation, is often cited as a key indicator of the presence of anisotropy within a layer directly above or below the boundary [*Levin and Park*, 1997a, 1997b; *Savage*, 1998]. Previous studies have attempted to model this in an attempt to constrain crustal anisotropy [*Savage*, 1998; *Levin and Park*, 2002; *Schulte-Pelkum et al*., 2005]. Other studies try to estimate the amount of splitting in *Ps* conversion (analogous to methods used on shear wave splitting in local or teleseismic earthquakes [e.g., *Silver and Chan*, 1991]) to constrain crustal anisotropy [*McNamara and Owens*, 1993; *Nagaya et al*., 2008, 2011], however, recent studies show that this can become unstable in the presence of noise [*Liu and Niu*, 2012]. Other studies have attempted to jointly invert receiver function data along with direct *S* waves (e.g., *SKS*/*SKKS* phases or *S* waves from local earthquakes) to better constrain the crustal anisotropy [*Levin et al*., 2008; *Obrebski et al*., 2010]. More recently, *Liu and Niu* [2012] combine the splitting methodology and analysis of the $cos2\theta$ variation to invert for crustal azimuthal anisotropy in receiver function data. Here I present a new, simple method for constraining crustal anisotropy, the anisotropic H-κ stacking technique.

3.1. Transverse Isotropy

To test the effects of anisotropy on Hκ, I generate a suite of horizontally transversely isotropic (HTI) and vertically transversely isotropic (VTI) models for varying amounts of anisotropy using the Matlab seismic anisotropy toolbox (MSAT) [*Walker and Wookey*, 2012] and the theory of *Thomsen* [1986]. These elastic constants are used to generate synthetic seismograms using the technique of *Angus and Thomson* [2012] which solves the reflection and transmission coefficients for discontinuous generally anisotropic media. All discontinuities are assumed to be horizontal. The synthetic seismograms are processed using deconvolution in the time domain [*Ligorria and Ammon*, 1999] with a maximum frequency of 0.67 Hz. Finally, the H-κ stacking technique is performed following the methods outlined in *Hammond et al*. [2011]. The models consist of a 30 km thick layer ($V_P = 6.5$ km s^{-1}, $V_S = 3.6$ km s^{-1}, $V_P/V_S = 1.81$, and $\rho = 2800$ kg m^{-3}), over a half-space ($V_P = 8.1$ km s^{-1}, $V_S = 4.5$ km s^{-1}, $V_P/V_S = 1.79$, and $\rho = 3200$ kg m^{-3}; Supporting Information Table S1). 1 invoke anisotropies in the upper layer of varying amounts, where anisotropy is defined by the peak-to-peak variation in velocity and the axis of symmetry defines the slow axis, a model synonymous with aligned fractures or fluid filled inclusions. I generate synthetic receiver functions across a range of back azimuths (10°–180°) and slownesses (equivalent to earthquakes from 40°, 60°, and 80° distance) and investigate both the slowness and back azimuthal dependence of Hκ as well as the Hκ estimates based on stacking data from many back azimuths and slownesses (synonymous with stacking all data from many back azimuths and slownesses in a real experiment). An important factor in accurately determining the correct values of *H* and κ is the assumption of the average V_P in the layer. In this study, I calculate the isotropic component of the *P* wave velocity for the elastic constants used in the model as the average *P* wave velocity in the crust (Supporting Information Table S1).

Figure 2 shows a model with 9.1% HTI anisotropy. It is evident that considerable variation in the arrival time and amplitude of receiver functions is present on both the transverse and radial components. In this study,

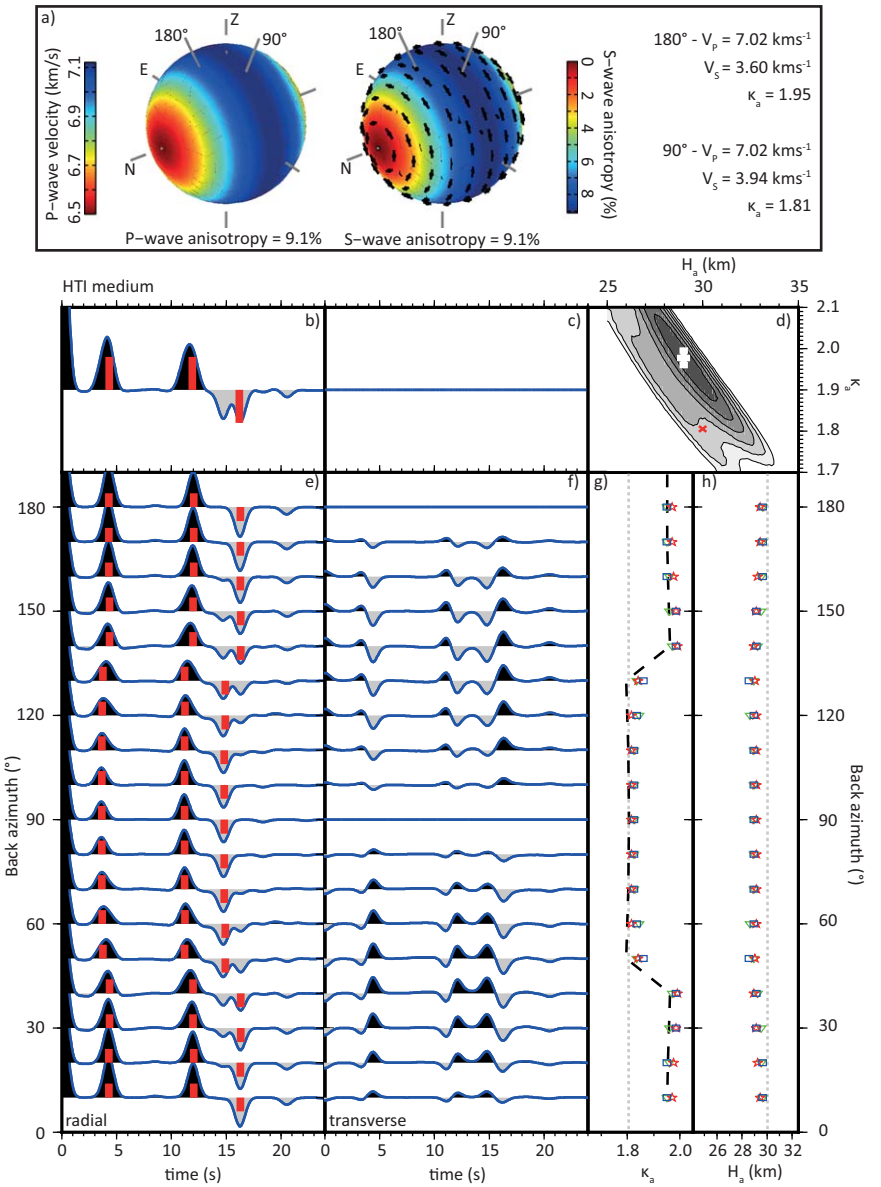

Figure 2. (a) The anisotropic model for a simple hexagonal medium with the symmetry plane (slow axis) normal to the *N* direction (HTI anisotropy). The left sphere shows the *P* wave velocity variations and the right sphere shows the *S* wave anisotropy variations. Black ticks show the polarization of the fast shear wave. Gray lines show the incidence angles for an incoming *P* wave from 60°. (b) Stacked radial receiver function for all data across all back azimuths and slowness. (c) Stacked transverse receiver function across all back azimuths and slownesses. (d) The Hκ result using all data across all back azimuths and slownesses. The red cross shows the isotropic crustal parameters (H = 30 km, κ = 1.81). (e) Individual radial receiver functions for different back azimuths (assuming an epicentral distance of 60°). Red lines show the arrival times of the *Ps* phase and subsequent multiples estimated from the best fitting Hκ result. (f) Individual transverse receiver functions for different back azimuths (assuming an epicentral distance of 60°). (g) Estimates of κ_a derived from Hκ on the individual back azimuth results. (h) Estimates of H_a derived from Hκ on the individual back azimuth results. The inverted triangle, square, and star relate to Hκ results from earthquakes of distance 40°, 60°, and 80°, respectively.

I am interested in the effects of anisotropy on Hκ, so I will focus on variations in the radial component. The anisotropy causes significant effects on the waveforms, giving rise to broad and multiple peaks on the radial component. This occurs because the *P*-to-*s* conversion that occurs at the discontinuity now creates two shear waves, Ps_1 and Ps_2. Ps_1 has its particle motion in the fast shear wave direction and Ps_2 is oriented perpendicular to this, thus travels slower (Figure 1). This is analogous to shear wave splitting often seen in *S* waves traveling through anisotropic media [e.g., *Silver*, 1996]. Due to this, significant variation in V_P/V_S is seen across all back azimuths ranging between 1.80 and 1.98. Little variation is observed in estimates of *H*

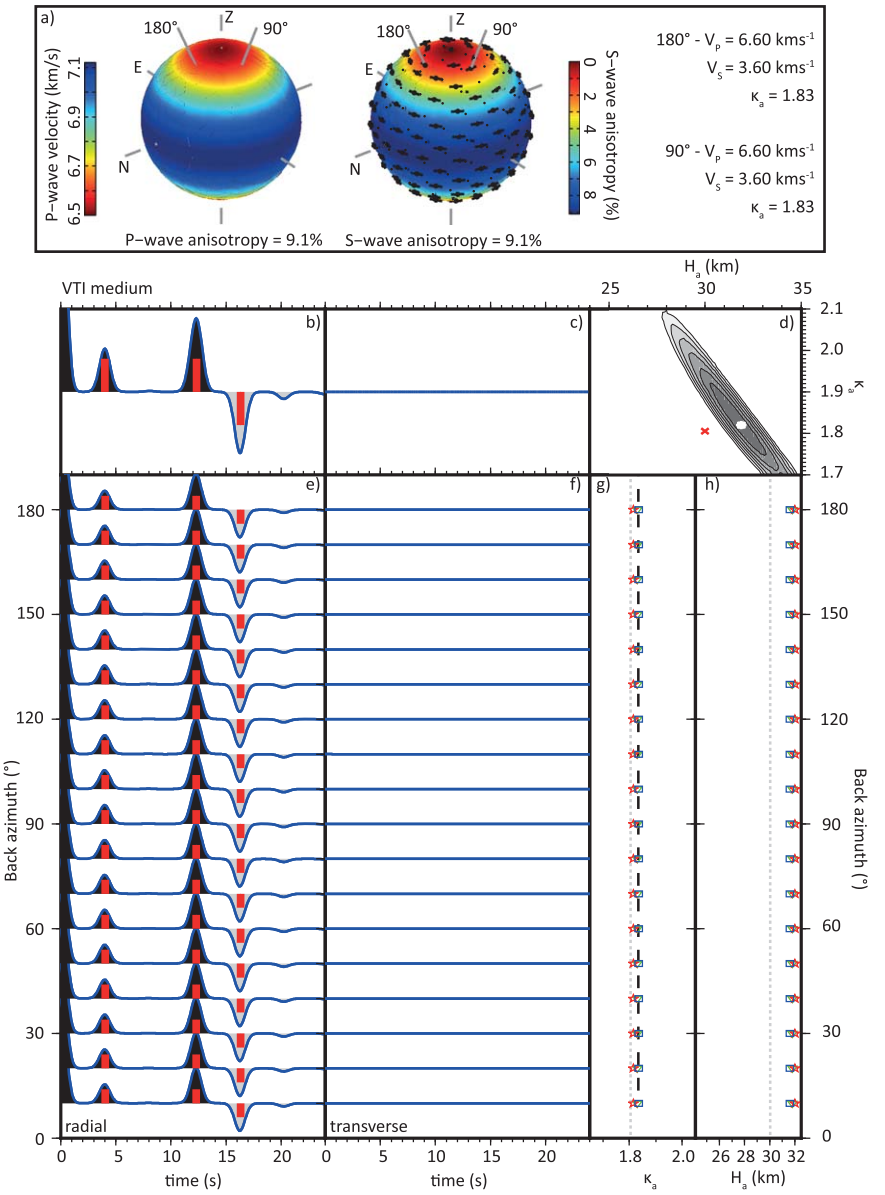

Figure 3. (a) The anisotropic model for a simple hexagonal medium with the symmetry plane (slow axis) normal to the *Z* direction (VTI anisotropy). See Figure 2 for details of other plots.

(28.9–29.6 km); however, when assuming the isotropic velocity of the elastic constants as the average *P* wave velocity, the thickness of the layer is underestimated. Little variation is seen as a function of slowness. Finally, summing all data across all back azimuths and slownesses produces an estimate of *H* which is too low (29.5 $\pm$ 0.1 km) and a high value of V_P/V_S (1.96 $\pm$ 0.02).

Figure 3 shows a model with 9.1% VTI anisotropy. No variation with back azimuth or slowness is observed in the radial receiver function waveform and no energy is observed on the transverse component, as expected for a case with a vertical symmetry axis. However, in this case, the estimated V_P/V_S is systematically too high (1.82 $\pm$ 0.00) and the thickness of *H* is overestimated (31.9 $\pm$ 0.0 km).

Due to the characteristic variations in V_P/V_S, I term these measurements of V_P/V_S the apparent V_P/V_S or κ_a. It is important to note that these estimates are not a measure of the true V_P/V_S of the medium, but are rather a result of significant anisotropy.

The reasons for the characteristic estimates of *H* and κ_a are clear when anisotropy is considered. The incoming *P* wave is sensitive to the apparent velocity in the near-vertical orientation (Figures 2 and 3). In the case

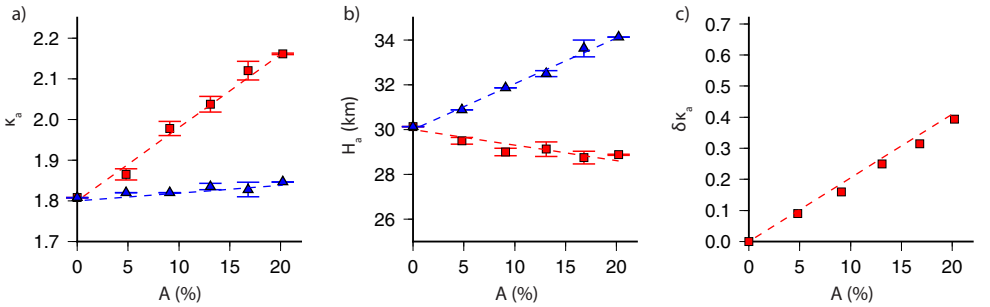

Figure 4. (a) Apparent V_P/V_S (κ_a) for estimates based on stacking data from all back azimuths and slownesses as a function of anisotropy (A) for HTI (red squares) and VTI (blue triangles) anisotropy. (b) Estimates of crustal thickness (H) based on stacking data from all back azimuths and slownesses as a function of anisotropy (A) for HTI (red squares) and VTI (blue triangles) anisotropy. (c) Maximum variation in κ_a ($\delta\kappa_a$) for HTI anisotropy as a function of anisotropy (A).

of an HTI medium, this will be close to the fast axis of the medium and in the case of a VTI medium, the slow axis. This means that the estimate for the average *P* wave velocity based on the isotropic opponent of the crust will be too low for an HTI case and too high for a VTI case. This gives rise to the errors in estimating *H*. The *Ps* conversions will be sensitive to the anisotropy for a near-vertical arrival. For an HTI medium anisotropy is high, thus causing shear wave splitting and the relative amplitudes of the two split shear waves (Ps_1 and Ps_2, Figure 1) depends on the incoming polarization of the phase. In the modeled example, the symmetry axis (slow direction) is oriented at 0°. A *P* wave arriving from this back azimuth will generate a *Ps* conversion with all the energy on the radial component and the shear wave will travel with a slower velocity (Figure 2). This gives rise to an estimate of V_P/V_S which is much higher than the isotropic value (Figure 2). Conversely, a *P* wave arriving from 90° will generate a shear wave which travels with the fast axis velocity, and thus the estimated V_P/V_S will be much lower (Figure 2). For back azimuths closer to the fast direction Ps_1, the fast Ps arrival, will have a stronger amplitude thus will stack more coherently and thus will dominate the Hκ stack. For back azimuths closer to the slow direction, the opposite will occur. The transition between the high and low values of κ_a is 45° from the anisotropy symmetry axis and the fast direction is defined by the lowest values of κ_a.

In a VTI medium, the anisotropy for a Ps conversion is very low and thus the *Ps* conversions will not generate any split shear waves. However, the vertically polarized shear wave will always travel with a slower velocity (Figure 3). As a result, the κ_a will always be higher, although due to the slower *P* wave velocity in the near-vertical orientation the effect will not be as dramatic as for an HTI medium.

I test a suite of anisotropic models with percentage anisotropy varying from 0 to 25% (Figure 4). In all models, the effects of anisotropy are similar to that described above, with more dramatic effects for high anisotropies.

These models show that anisotropy will have a significant impact on the estimates of crustal thickness and V_P/V_S derived from Hκ, and thus, in an anisotropic medium, caution must be taken when using κ as a proxy for crustal composition.

3.2. Melt-Induced Anisotropy

The previous section shows the general anisotropic case, however, in reality, mechanisms such as the preferential alignment of melt may have more complex anisotropic signatures [*Kendall*, 1994]. To test this, we model the case of anisotropy caused by the preferential alignment of melt inclusions. Using MSAT, I generate elastic constants using the effective medium theory of *Tandon and Weng* [1984] for a suite of models with varying melt fractions and aspect ratios (a measure of the geometry of the inclusion, where low numbers indicate flat discs and numbers approaching one correspond to spherical inclusions). The models have a background matrix with $V_P = 6.5$ km s^{-1}, $V_S = 3.6$ km s^{-1}, $\rho = 2700$ kg m^{-3} and melt inclusions with $V_P = 2.7$ km s^{-1}, $V_S = 0.0$ km s^{-1}, $\rho = 2700$ kg m^{-3}. The models assume that the inclusions are isolated within the matrix.

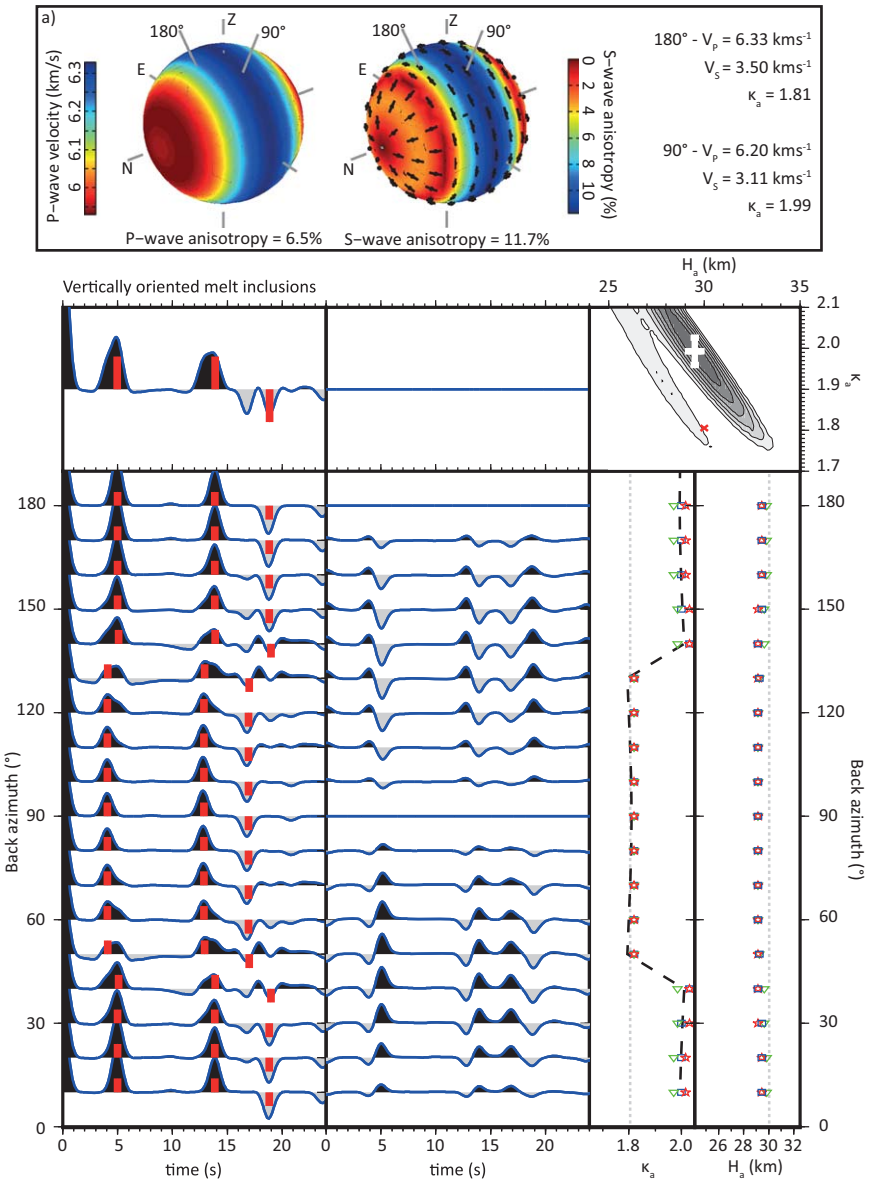

Figure 5. (a) The anisotropic model for 5% melt in vertically oriented isolated disks of aspect ratio 0.1 with the symmetry axis normal to the *Z* plane. See Figure 2 for details of other plots.

Figures 5 and 6 show the case for a medium with 5% melt in inclusions with an aspect ratio of 0.1 oriented vertically and horizontally, respectively. Similar variations in κ_a and *H* are seen to that observed for the transverse isotropy cases discussed previously. However, for the melt-induced anisotropy case, the effects are larger as melt has a larger effect on the *S* wave anisotropy compared to the *P* wave (Figures 5 and 6). This means that for receiver functions estimated from events along the slow axis in a medium with vertically oriented inclusions, the κ_a will be larger than for the simple HTI case discussed previously, and for a medium with horizontally aligned melt inclusions, the κ_a across all back azimuths will be larger than for the simple VTI case discussed previously. This may explain why high estimates of κ are often seen in volcanic settings, and shows that it is important to consider the anisotropic mechanism to fully understand anisotropic Hκ.

I test a suite of models with melt fractions varying from 1 to 7% and aspect ratios from 0.02 to 0.2 (Supporting Information Table S2). In all models, the effects of anisotropy are similar to that described above, with more dramatic effects for high melt fractions and lower aspect ratios (Figure 7). There is a clear trade-off

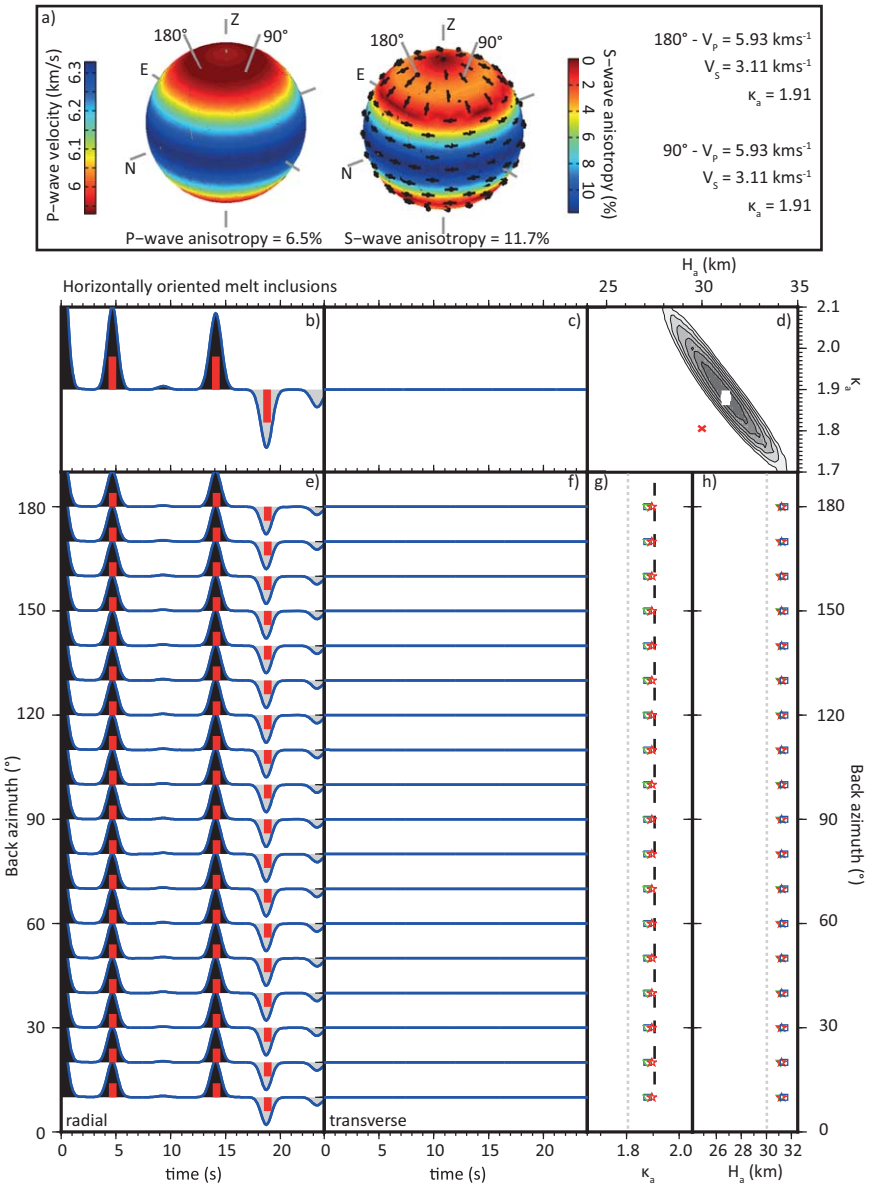

Figure 6. (a) The anisotropic model for 5% melt in horizontally oriented isolated disks of aspect ratio 0.1 with the symmetry axis normal to the *Z* plane. See Figure 2 for details of other plots.

between melt fractions and aspect ratios as has been discussed previously [e.g., *Blackman and Kendall*, 1997; *Hammond and Humphreys*, 2000; *Holtzman and Kendall*, 2010], but the characteristic trends here show that with suitable data (i.e., good back azimuthal coverage) it may be possible to place constraints on the melt fractions and geometries in the crust beneath volcanic regions.

4. Anisotropic H-κ Stacking

The characteristic variation in κ_a as a function of back azimuth means that it is possible to invert receiver function data to place constraints on the amount, and characteristics of anisotropy in the crust beneath a seismic station. Many receiver function studies have estimated high κ beneath the Main Ethiopian Rift (MER) and Afar Depression, Ethiopia [*Dugda et al.*, 2005; *Stuart et al.*, 2006; *Hammond et al.*, 2011]. The estimates of κ can be much higher than 2, and are interpreted as been caused by melt within the crust beneath

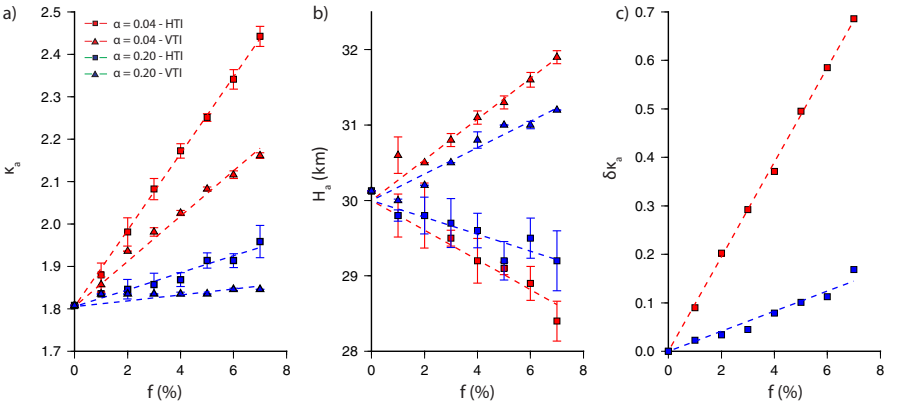

Figure 7. (a) Apparent V_P/V_S (κ_a) for estimates based on stacking data from all back azimuths and slownesses as a function of melt fraction (f) for vertically oriented melt (squares) and horizontally oriented melt (triangles) and for aspect ratios of 0.04 (red) and 0.2 (blue). (b) Estimates of crustal thickness (H) based on stacking data from all back azimuths and slownesses as a function of melt fraction (f) for vertically oriented melt (squares) and horizontally oriented melt (triangles) and for aspect ratios of 0.04 (red) and 0.2 (blue). (c) Maximum variation in κ_a ($\delta\kappa_a$) for vertically oriented melt as a function of melt fraction for aspect ratios of 0.04 (red) and 0.2 (blue).

the MER and Afar Depression [*Dugda et al*., 2005; *Stuart et al*., 2006; *Hammond et al*., 2011]. Additional evidence for melt comes from recent magnetotelluric studies, which show evidence for considerable (<13%) melt fractions in the crust [*Desissa et al*., 2013], the identification of crustal magma chambers from petrology [*Field et al*., 2013], and low velocities and high anisotropy in the crust from seismology [*Hammond et al*., 2011; *Keir et al*., 2011; *Guidarelli et al*., 2011]. The presence of multiple dike injections [*Belachew et al*., 2011] along with many subsidence and inflation signals [*Grandin et al*., 2010; *Wright et al*., 2012] also suggest that both vertically oriented melts (dikes) and horizontally oriented melts (sills) are present and interacted during the recent rifting episode [*Grandin et al*., 2010; *Wright et al*., 2012]. As a result, the Afar Depression and in particular the region around the recent series of dike intrusions at Dabbahu-Manda Hararo (DMH; Figure 8) is an ideal area to try anisotropic Hκ.

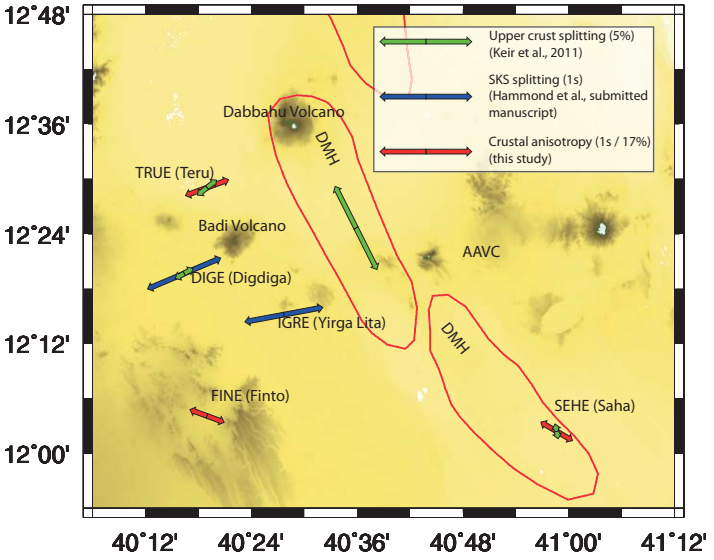

Figure 8. Map showing the Dabbahu-Manda Hararo magmatic segment and surrounding area. Red lines mark out the volcanic segments. Green arrows show the upper crustal shear wave splitting results of *Keir et al*. [2011]. Blue arrows show the upper mantle shear wave splitting results of Hammond et al. (submitted manuscript). Red arrows show the orientation of melt inclusions in the crust constrained from this study, where crustal splitting is estimated for near-vertical shear waves and assuming the crustal thickness estimated by *Hammond et al*. [2011]. Note the different scale for the upper crustal anisotropy and the other measurements. DMH = Dabbahu-Manda Hararo magmatic segment, AAVC = Ado Ale Volcanic Complex.

To invert the Afar data, I perform a grid search across a suite of elastic constants for vertically and horizontally oriented melt. I vary the aspect ratio from 0.02 to 1.0 and melt fraction from 0 to 14% (where 0% melt is the equivalent to having no melt). I also include two additional cases for vertical inclusions and horizontal inclusions only. Table 1 shows the parameters used in the grid search, note the nonlinear parameterization for the aspect ratio due to large variations in anisotropy at low aspect ratio compared to higher ones. Where both horizontal and vertical inclusions are included I average the HTI and VTI elastic constants to create a composite medium. I test different symmetry axes by rotating the elastic constants in the horizontal plane from 0° to 180° in 10° intervals. Using the elastic constants I estimate the *P* wave velocity and the two *S* wave velocities required to estimate the κ_a for a suite of back azimuths (assuming an earthquake from 60° distance). If the incoming back azimuth is $\leq$45° from the fast axis, then the fast *S* wave velocity is used together with the *P* wave velocity to estimate κ_a. If the incoming back azimuth is $>$45° from the fast axis, then the slow *S* wave velocity is used instead. Figures 2–6 show that this method reproduces the results of the synthetic tests well (the black dashed line shows estimates using this technique compared to those estimated from synthetic seismograms). I do not try to match the H_a as this shows little variation as a function of back azimuth. This method means that synthetic seismograms are not required to model the back azimuthal variation in the κ_a, and thus a large number of models (211,428) can be efficiently tested. I estimate a χ^2 misfit from the modeled κ_a and the observed κ_a (along with the bootstrap errors for the data derived κ_a). In these inversions, there are six parameters; melt fraction, aspect ratio for both vertical and horizontal inclusions, orientation of the vertical inclusions, and the two cases where horizontal and vertical inclusions independently. I set a χ^2 value of 12.59 (given the six degrees of freedom in this model). All models which have misfits below this value are assumed to fit the data within the 95% confidence interval. An assumption in these models is that the discontinuities are horizontal. Dipping layers can affect the arrival times of *Ps* conversions on both the radial and transverse components [*Liu and Niu*, 2012] and so care must be taken if dipping layers are expected.

To test the inversion technique, I construct a model based on a combination of sill and dike-like structures in the crust, a model often proposed for melt storage in the crust [e.g., *Maclennan et al*., 2001; *Annen et al*., 2006; *Blundy and Cashman*, 2008]. I build a model with 6% melt in horizontally aligned melt inclusions with aspect ratio 0.04 and 6% melt in vertically aligned melt inclusions with aspect ratio of 0.1 (Figure 9). 1 generate synthetic receiver functions across back azimuths from 10° to 180° and estimate κ_a using Hκ. I impose errors in κ_a of 0.02, similar to errors seen for well-constrained Hκ results [*Hammond et al*., 2011]. I use this as the data set in the inversion. It is evident that this inversion technique can resolve the aspect ratios of the horizontal inclusions and orientation of the vertical inclusions well; however, there is a trade-off between aspect ratio and melt fraction meaning that melt faction and aspect ratio for vertical inclusions are less well constrained (Figure 9).

5. Constraints on Melt Storage Beneath the Afar Depression

Three stations (SEHE, FINE, and TRUE) in the vicinity of DMH have data of high enough quality from enough back azimuths to be suitable for anisotropic Hκ (see *Hammond et al*. [2011] for more details). I stack the data in 20° bins, overlapping by 10°. The Hκ technique relies on the *Ps*, *PpPs*, and *PsPs*/*PpSs* phases being evident above the noise level and so I impose a minimum of four events per back azimuthal bin for each back azimuthal stack (see Figures 10–12, for details).

Figures 10–12 and Table 2 show the inversion results for SEHE, FINE, and TRUE. Similar to the synthetic test (Figure 9), it is possible to place constraints on the aspect ratio of the horizontal inclusions and the orientation of the vertical inclusions. These parameters offer valuable insights into the plumbing system beneath the DMH volcanic system. The first observation is that both vertical and horizontal inclusions must be present. The back azimuthal variation can only be fit with vertical inclusions, and the consistently high κ_a requires the horizontal inclusions. For all three stations, the aspect ratio of the horizontal inclusions must be lower than 0.07. These very low aspect ratios suggest that wide, very thin inclusions must be present in the crust beneath Afar. *Hammond et al*. [2011], *Guidarelli et al*. [2011], and *Desissa et al*. [2013] show that a large proportion of the partial melt beneath Afar is stored in the lower crust and uppermost mantle, thus this result suggests that melt is stored in sill-like features in the lower crust beneath Afar. There must be a number of sills at variable depths (stacked sills) to generate the anisotropy (Figure 13). The recent

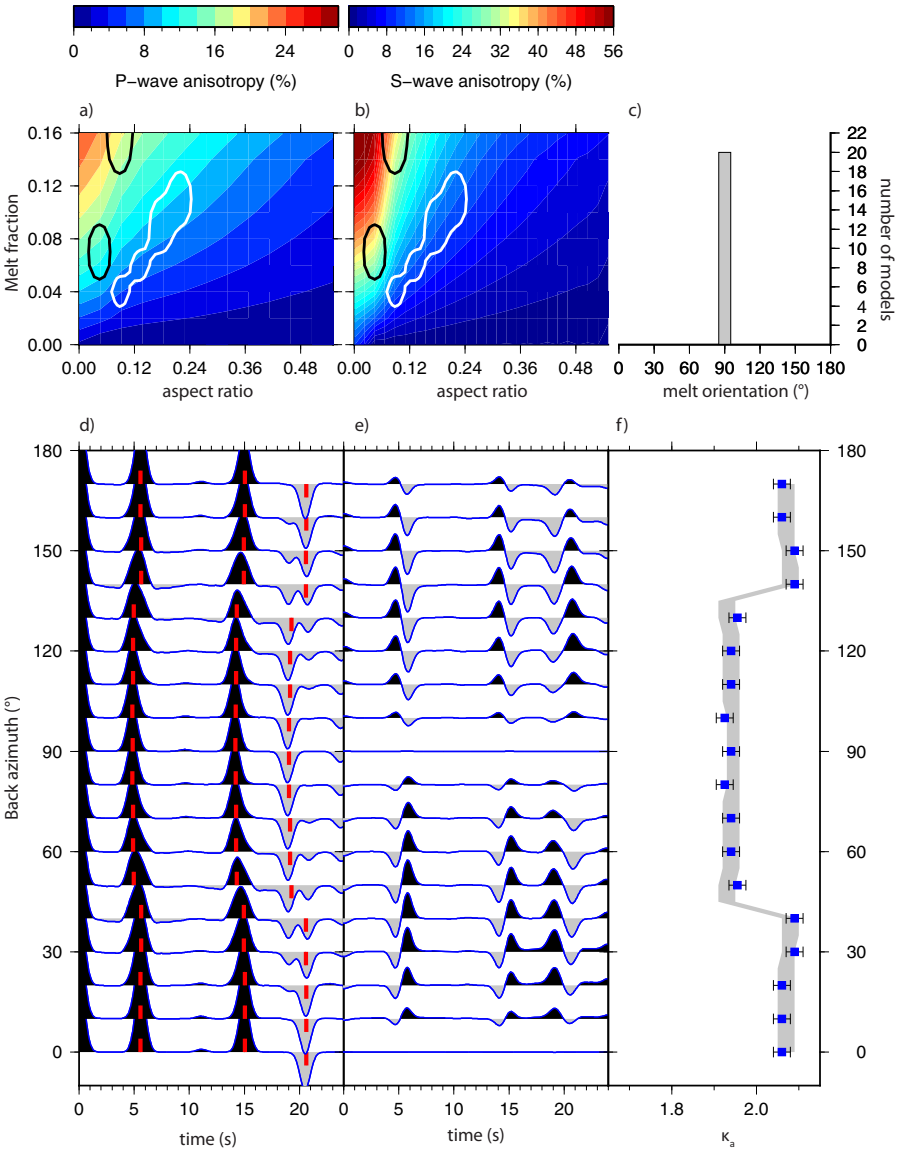

Figure 9. The anisotropic Hκ results for a synthetic test. The input model has 6% melt in horizontal inclusions with aspect ratio of 0.08 and vertical inclusions with aspect ratio of 0.12. (a) The range of models which fit the χ^2 misfit criteria. The black contour shows the models for horizontally aligned inclusions and the white contour shows the models for the vertically aligned inclusions. The color contours underneath show maximum *P* wave anisotropy for the range of models searched. (b) The same as Figure 9a, but with *S* wave anisotropy shown by the colored contours. (c) Histogram showing the orientation of the vertical inclusions for all models which pass the χ^2 misfit criteria. (d) Individual radial receiver functions for different back azimuths (assuming an epicentral distance of 60°) for the input model. Red lines show the arrival times of the *Ps* phase and subsequent multiples estimated from the best fitting Hκ result. (e) Individual transverse receiver functions for different back azimuths (assuming an epicentral distance of 60°) for the input model. (f) The Hκ results for individual back azimuths (blue squares). The gray shaded region shows the range of theoretical κ_a curves based on the models which pass the χ^2 misfit criteria.

magnetotelluric studies beneath Afar show a ~40 km wide region of high conductivities inferred as melt in the lower crust [*Desissa et al.*, 2013]. If this region is comprised of stacked sills, then assuming a 40 km wide sill with aspect ratio of 0.07 gives a maximum sill thickness of 2.8 km.

The inversions also identify the presence of vertically oriented inclusions beneath Afar. While the aspect ratio is not well constrained, it does suggest that the aspect ratios for the vertical inclusions are higher than the horizontal ones >0.05. Interestingly, the orientation of the vertical inclusions is quite variable beneath Afar. Beneath SEHE the oriented melt is aligned parallel to the strike of the dike intrusions (110–120°). Beneath FINE the melt is oriented in a similar direction (100–120°), but beneath TRUE the melt is oriented

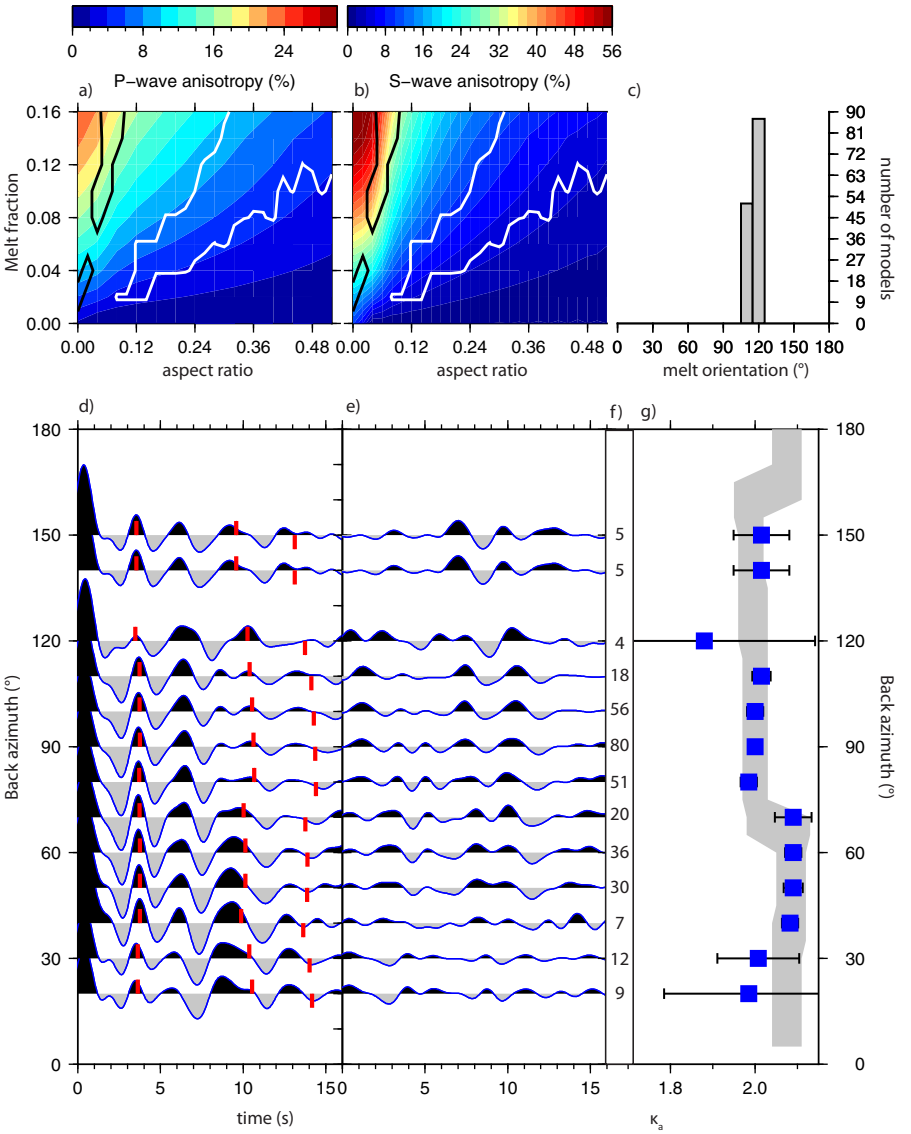

Figure 10. The anisotropic Hκ results for station SEHE. (a) The range of models which fit the χ^2 misfit criteria. The black contour shows the models for horizontally aligned inclusions and the white contour shows the models for the vertically aligned inclusions. The color contours underneath show maximum *P* wave anisotropy for the range of models searched. (b) The same as Figure 10a, but with *S* wave anisotropy shown by the colored contours. (c) Histogram showing the orientation of the vertical inclusions for all models which pass the χ^2 misfit criteria. (d) Back azimuth stacks of radial receiver functions. Red lines show the arrival times of the *Ps* phase and subsequent multiples estimated from the best fitting Hκ result. (e) Back azimuth stacks of radial receiver functions. (f) Number of receiver functions in the back azimuthal stacks. (g) The Hκ results for individual back azimuths (blue squares). The gray shaded region shows the range of theoretical κ_a curves based on the models which pass the χ^2 misfit criteria.

perpendicular to the rift (60–70°). These orientations match the upper crustal anisotropy derived from upper crustal earthquakes [*Keir et al.*, 2011] and teleseismic data (Hammond et al., submitted manuscript), suggesting that melt is oriented along the strain field around DMH (Figure 8). Additional evidence of anisotropy comes in the form of energy on the transverse component. It is expected that a change in the polarity of the signal should occur at back azimuths equal to the fast direction (Figure 9). Due to the noisy signals on the transverse component it is hard to see if this is true for the three stations used. Noisy transverse energy is common in receiver function studies. This shows that the anisotropic Hκ stacking may be a more suitable technique for constraining crustal anisotropy than modeling the transverse component alone.

The magnitude of anisotropy shows major differences between the measurements of anisotropy determined by this method and those by shear wave splitting [*Keir et al.*, 2011; Hammond et al., submitted

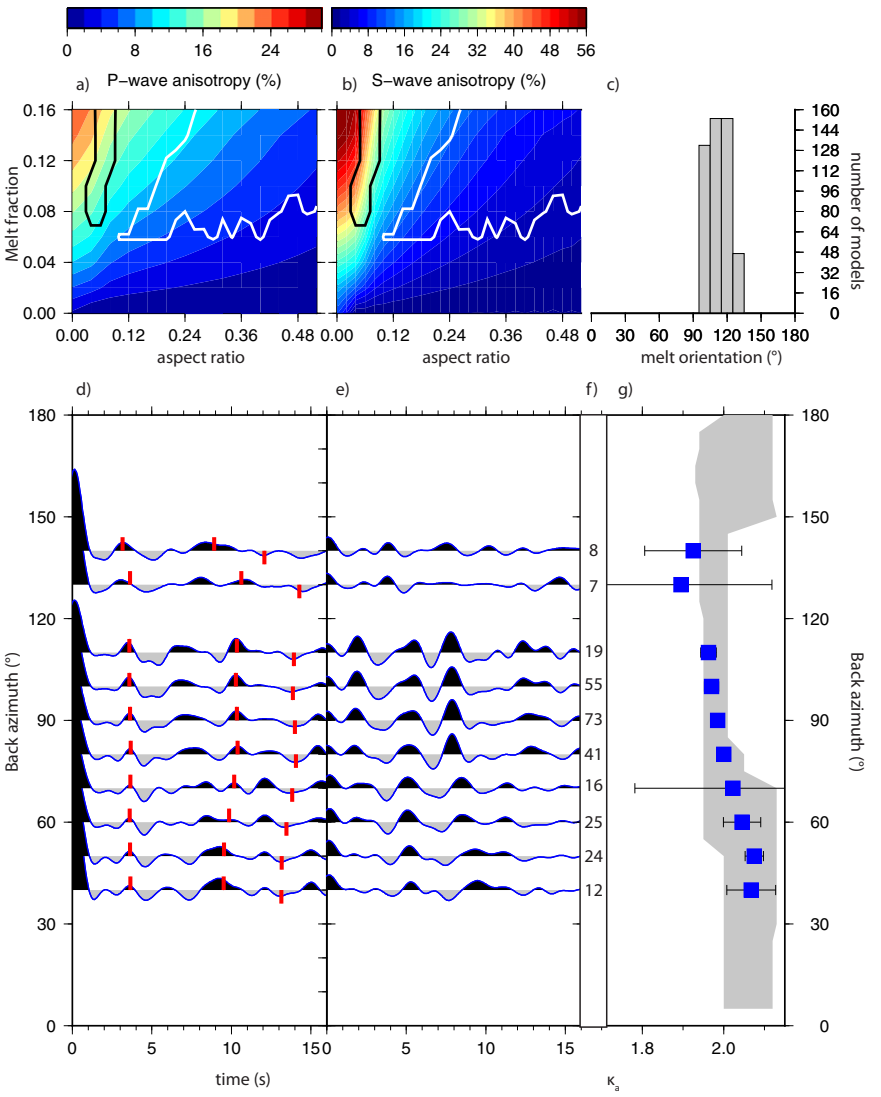

Figure 11. The anisotropic Hκ results for station FINE. See Figure 10 for details on all plots.

manuscript]. Anisotropy is estimated as $(V_{fast} - V_{slow})/V_{average}$, where V_{fast} is the fast wave speed, V_{slow} is the slow wave speed, and $V_{average}$ is the average wave speed. Crustal anisotropy measured from shear wave splitting in crustal earthquakes close to DMH is sensitive to the upper crust only (top 10 km) [*Keir et al.*, 2011] and shows anisotropies of 1–6%. However, the highest anisotropies are located where recent upper crustal dike injections were observed (Figure 8) [*Keir et al.*, 2011]. Away from this location average upper crustal anisotropy is closer to 1%. The magnitude of *S* wave anisotropy derived for near-vertically propagating shear waves through the whole crust is much larger (<10%; Figure 8). This supports the idea that melt is predominantly stored in the lower crust, except in the regions where dikes have recently been injected at DMH (Figure 8). Hammond et al. (submitted manuscript)] have conducted shear wave splitting on teleseismic data for Afar stations and show evidence for multiple layers of anisotropy beneath the Afar Depression. The orientation of the fast direction in the upper layer beneath Afar is very similar to that inferred from the anisotropic Hκ (Figure 8). The delay times for anisotropy in the upper layer are ~0.86 s. Anisotropy in the crust can explain a large portion of this signal (<0.5 s; Table 2 and Figure 8).

The region beneath SEHE has a long record of subsidence linked to the dike injections [*Grandin et al.*, 2010; *Wright et al.*, 2012], so it is likely that melt is flowing away from SEHE toward the region of dike injection. Interestingly, the orientation of melt and stress field beneath TRUE points from a region of large melt

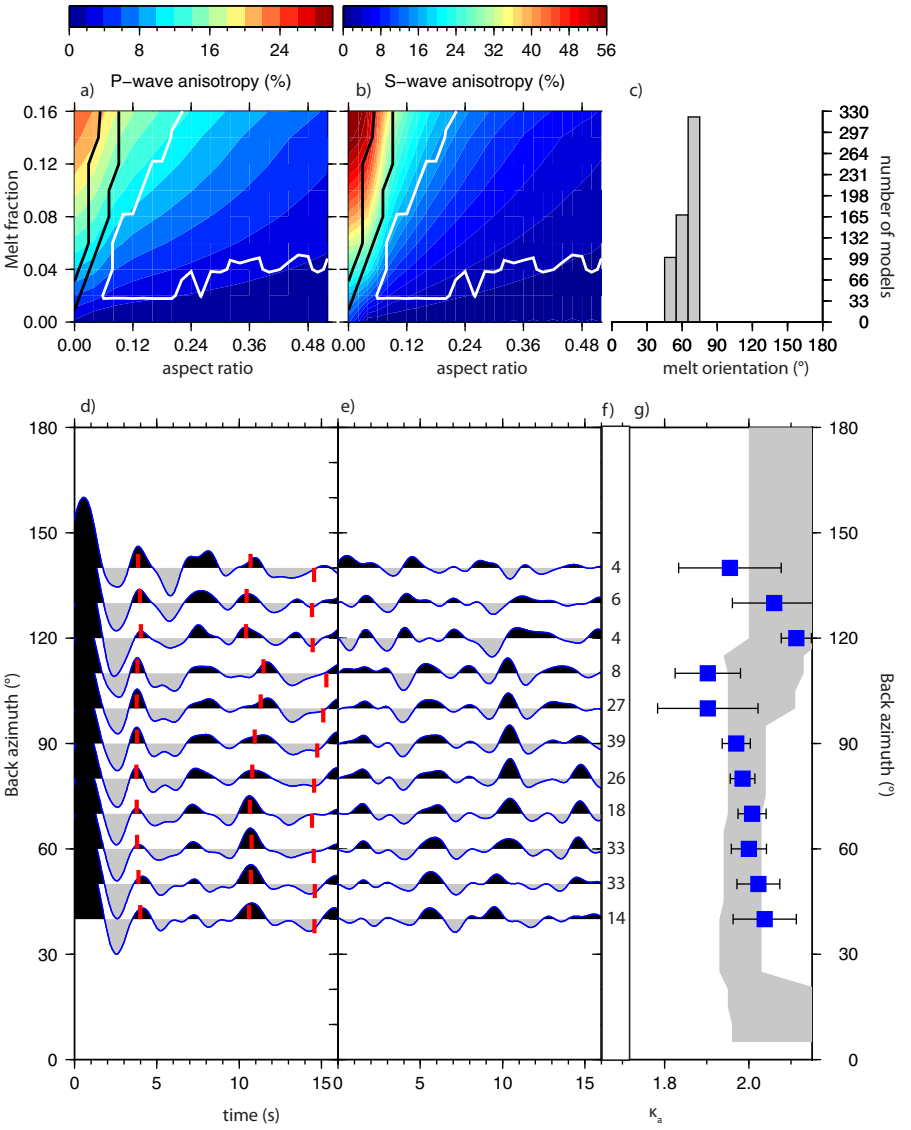

Figure 12. The anisotropic Hκ results for station TRUE. See Figure 10 for details on all plots.

storage (as seen in the magnetotellurics) [*Desissa et al.*, 2013] toward Dabbahu, the volcano at the northern tip of the DMH volcanic segment and a volcano which has shown multiple magma chambers from petrological and Insar studies [*Grandin et al.*, 2011; *Wright et al.*, 2012; *Field et al.*, 2013]. Also, the fast directions from the teleseismic data point toward the region where multiple dikes have been injected. This suggests that melt may be fed to the volcanoes and dikes from off-axis lower crustal reservoirs.

Table 2. Table Showing the Models Which Pass the χ^2 Misfit Criteria for FINE (Finto), SEHE (Saha), and TRUE (Teru)[a]

		Horizontal Inclusions			Vertical Inclusions				
Station	Melt Fraction (%)	Aspect Ratio ($\times 10^{-2}$)	*P* Wave Anisotropy (%)	*S* Wave Anisotropy (%)	Aspect Ratio ($\times 10^{-2}$)	Orientation (°)	*P* Wave Anisotropy (%)	*S* Wave Anisotropy (%)	Crustal Splitting (s)
FINE	3–16	2–9	10–19	29–40	6–70	100–130	2–10	2–12	0.1–0.4
SEHE	2–16	1–8	10–19	29–42	8–60	110–120	2–9	3–10	0.1–0.4
TRUE	2–16	1–9	10–21	29–45	5–90	50–70	1–12	1–16	0.0–0.5

[a]The range of crustal splitting estimates are calculated for vertically propagating shear wave through the models assuming the crustal thicknesses estimated by *Hammond et al.* [2011].

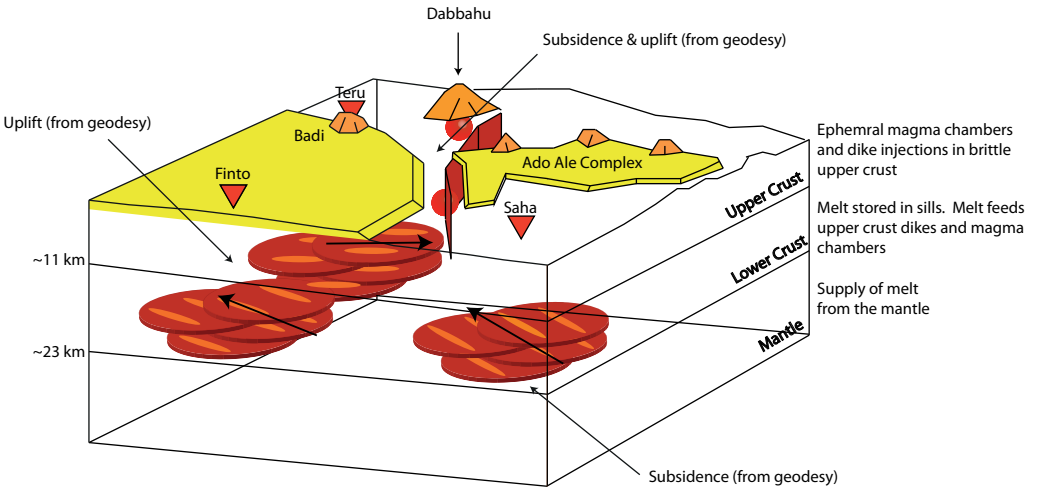

Figure 13. Conceptual model for the magmatic plumbing system around the Dabbahu-Manda Hararo rift segment. Melt in the lower crust is likely stored in stacked sills with some vertically oriented melt connecting these sills. The vertically oriented melt is aligned with the strain around DMH and may highlight the orientation of flow beneath this region. It suggests that off-axis lower crustal melt storage regions may feed the upper crustal magma chambers and dike injections beneath the rift axis.

6. Conclusions

In summary, the major conclusions of this study are:

1. In an anisotropic medium, Hκ measures the apparent V_P/V_S which is a function of the anisotropy characteristics.

2. For an HTI medium, κ_a varies as a function of back azimuth with lower κ_a at back azimuths corresponding to the fast direction and higher κ_a for back azimuths perpendicular to these.

3. The variation in κ_a is proportional to the amount of anisotropy in an HTI medium.

4. The transition from high κ_a to low κ_a occurs 45° from the symmetry axis with the low values of κ_a defining the fast axis.

5. For a VTI medium, κ_a is consistently higher than the isotropic κ across all back azimuths, but estimating anisotropy is more difficult as it requires an assumption of the true κ.

6. For an HTI medium, H_a can be an underestimate of the true H if an isotropic average P wave velocity is assumed.

7. For an VTI medium, H_a can be an overestimate of the true H if an isotropic average P wave velocity is assumed.

8. For melt-induced anisotropy, the patterns are similar to the HTI and VTI cases above, but with stronger affects due to larger S wave anisotropy relative to the P wave anisotropy.

9. A combination of VTI and HTI anisotropy will retain the characteristics of both, increasing κ_a across all back azimuths while retaining the variation in κ_a as a function of back azimuth.

10. The characteristic trends in κ_a allow data to be inverted for the anisotropic characteristics.

11. Beneath Afar melt is stored in interconnected stacked sills in the lower crust with low aspect ratios and a maximum thickness of 2.8 km (Figure 13).

12. The melt beneath Afar is likely mobile with shallow magma chambers and upper crustal dikes fed by off-axis lower crustal magma storage regions (Figure 13).

It is clear that anisotropy is an important consideration when performing Hκ and in the presence of anisotropy the values of κ measured are in fact apparent measurements which are harder to relate to composition of the crust. Investigating back azimuthal variations in κ is key to fully understand the composition and

nature of the crust using receiver functions. Other techniques to measure anisotropy in the crust may give good constraints but are limited in their applicability. Surface waves lack the lateral resolution [*Montagner*, 1998], shear wave splitting relies on a good distribution of seismicity in the lower crust [*Kaneshima*, 1990] to constrain anisotropy across the whole crust, or complex analysis to pull apart anisotropy in teleseismic phases [*Abt and Fischer*, 2008; *Wookey*, 2012]. The anisotropic Hκ allows constraints on the anisotropic characteristics of the whole crust to be determined from receiver functions, providing good lateral and depth resolution everywhere a seismic station is deployed.

In this study, I have applied a new anisotropic H-κ stacking technique to melt beneath the Afar Depression, but in fact this technique could constrain crustal anisotropy beneath any setting. Hκ has shown evidence for high κ ($>$1.9) beneath transform faults [*Ozacar and Zandt*, 2009; *Ozacar et al*., 2010], mountain building regions [*Xu et al*., 2007, 2013] and other volcanic settings [*Ai et al*., 2005; *Eagar et al*., 2011; *Yang et al*., 2013]. In all these cases, melt has been invoked to explain the high values of κ. Using the anisotropic Hκ in these locations can better constrain the anisotropic mechanisms present and thus better highlight the presence/absence of melt and melt geometries, or the presence of any other anisotropic mechanism such as aligned minerals related to crustal deformation.

Acknowledgments

I would like to thank Doug Angus for providing the synthetic seismogram software and James Wookey for discussions about MSAT. Both, along with Mike Kendall are thanked for their comments on the draft manuscript. Karen Fisher and one anonymous review are also thanked for their comments, which helped improve the paper. The data collection in the Afar Depression were funded by NERC grants NE/E007414/1 and NE/D008611/1 and NSF grant EAR-0635789. All those involved in fieldwork are thanked for their efforts. Data collected are available through the IRIS Data Management Center. The facilities of the IRIS Consortium are supported by the National Science Foundation under Cooperative Agreement EAR-1063471, the NSF Office of Polar Programs and the DOE National Nuclear Security Administration. The facilities of the IRIS Data Management System, and specifically the IRIS Data Management Center, were used for access to waveform and metadata required in this study. The IRIS DMS is funded through the National Science Foundation and specifically the GEO Directorate through the Instrumentation and Facilities Program of the National Science Foundation under Cooperative Agreement EAR-1063471. All those involved in fieldwork are thanked for their efforts. J.O.S.H. is supported by NERC Fellowship NE/I020342/1.

References

Abers, G. A., X. Hu, and L. R. Sykes (1995), Source scaling of earthquakes in the Shumagin region, Alaska: Time-domain inversions of regional waveforms, *Geophys. J. Int.*, *123*, 41–58.

Abt, D. L., and K. M. Fischer (2008), Resolving three-dimensional anisotropic structure with shear wave splitting tomography, *Geophys. J. Int.*, *173*(3), 859–886.

Ai, Y., D. Zhao, X. Gao, and W. Xu (2005), The crust and upper mantle discontinuity structure beneath Alaska inferred from receiver functions, *Phys. Earth Planet. Inter.*, *150*(4), 339–350.

Ammon, C. J. (1991), The isolation of receiver effects from teleseismic P waveforms, *Bull. Seismol. Soc. Am.*, *81*, 2504–2510.

Angus, D. A., and C. J. Thomson (2012), Modelling converted seismic waveforms in isotropic and anisotropic 1-D gradients: Discontinuous versus continuous gradient representations, *Stud. Geophys. Geod.*, *56*(2), 383–409.

Annen, C., J. Blundy, and R. Sparks (2006), The genesis of intermediate and silicic magmas in deep crustal hot zones, *J. Petrol.*, *47*(3), 505–539.

Belachew, M., C. J. Ebinger, D. Cote, D. Keir, J. Rowland, J. O. S. Hammond, and A. Ayele (2011), Comparison of dike intrusions in an incipient seafloor spreading segment in Afar, Ethiopia: Seismicity perspectives, *J. Geophys. Res.*, *116*, B06405, doi:10.1029/2010JB007908.

Blackman, D. K., and J. Kendall (1997), Sensitivity of teleseismic body waves to mineral texture and melt in the mantle beneath a mid-ocean ridge, *Philos. Trans. R. Soc. London A*, *355*, 217–231.

Blundy, J., and K. Cashman (2008), Petrologic reconstruction of magmatic system variables and processes, *Rev. Mineral. Geochem.*, *69*(1), 179–239.

Desissa, M., N. E. Johnson, K. A. Whaler, S. Hautot, S. Fisseha, and G. Dawes (2013), Mantle magma reservoir imaged magnetotellurically beneath the proto-mid-ocean ridge in Afar, Ethiopia, *Nat. Geosci.*, *6*, 861–865.

Dugda, M. T., A. A. Nyblade, J. Julia, C. A. Langston, C. J. Ammon, and S. Simiyu (2005), Crustal structure in Ethiopia and Kenya from receiver function analysis: Implications for rift development in eastern Africa, *J. Geophys. Res.*, *110*, B01303, doi:10.1029/2004JB003065.

Eagar, K. C., M. J. Fouch, D. E. James, and R. W. Carlson (2011), Crustal structure beneath the High Lava Plains of eastern Oregon and surrounding regions from receiver function analysis, *J. Geophys. Res.*, *116*, B02313, doi:10.1029/2010JB007795.

Field, L., J. Blundy, A. Calvert, and G. Yirgu (2013), Magmatic history of Dabbahu: A composite volcano in the Afar Rift, Ethiopia, *Geol. Soc. Am. Bull.*, *125*(1–2), 128–147.

Grandin, R., A. Socquet, M. P. Doin, E. Jacques, J. B. de Chabalier, and G. C. P. King (2010), Transient rift opening in response to multiple dike injections in the Manda Hararo rift (Afar, Ethiopia) imaged by time-dependent elastic inversion of interferometric synthetic aperture radar data, *J. Geophys. Res.*, *115*, B09403, doi:10.1029/2009JB006883.

Grandin, R., E. Jacques, A. Nercessian, A. Ayele, C. Doubre, A. Socquet, D. Keir, M. Kassim, A. Lemarchand, and G. C. P. King (2011), Seismicity during lateral dike propagation: Insights from new data in the recent Manda Hararo-Dabbahu rifting episode (Afar, Ethiopia), *Geochem. Geophys. Geosyst.*, *12*, Q0AB08, doi:10.1029/2010GC003434.

Guidarelli, M., G. Stuart, J. O. S. Hammond, J. Kendall, A. Ayele, and M. Belachew (2011), Surface wave tomography across Afar, Ethiopia: Crustal structure at a rift triple-junction zone, *Geophys. Res. Lett.*, *38*, L24313, doi:10.1029/2011GL046840.

Gupta, S. (2003), The nature of the crust in southern India: Implications for Precambrian crustal evolution, *Geophys. Res. Lett.*, *30*(8), 1419, doi:10.1029/2002GL016770.

Gurrola, H., G. E. Baker, and J. B. Minster (1995), Simultaneous time-domain deconvolution with application to the computation of receiver functions, *Geophys. J. Int.*, *120*, 537–543.

Hammond, J. O. S., J. Kendall, G. W. Stuart, D. Keir, C. J. Ebinger, A. Ayele, and M. Belachew (2011), The nature of the crust beneath the Afar triple junction: Evidence from receiver functions, *Geochem. Geophys. Geosyst.*, *12*, Q12004, doi:10.1029/2011GC003738.

Hammond, J. O. S., J-M. Kendall, J. Wookey, G. W. Stuart, D. Keir, and A. Ayele (2014), Towards differentiating flow, melt or fossil seismic anisotropy beneath Ethiopia, *Geochem. Geophys. Geosys*.

Hammond, W., and E. Humphreys (2000), Upper mantle seismic wave velocity: Effects of realistic partial melt geometries, *J. Geophys. Res.*, *105*, 10,975–10,986.

Helffrich, G. (2006), Extended-time multi-taper frequency domain cross-correlation receiver function estimation, *Bull. Seismol. Soc. Am.*, *96*, 344–347.

Holtzman, B. K., and J. Kendall (2010), Organized melt, seismic anisotropy and plate boundary lubrication, *Geochem. Geophys. Geosyst.*, *11*, Q0AB06, doi:10.1029/2010GC003296.

Kaneshima, S. (1990), Origin of crustal anisotropy: ShearWave splitting studies in Japan, *J. Geophys. Res.*, *95*, 11,121–11,133.

Keir, D., M. Belachew, C. J. Ebinger, J. Kendall, J. O. S. Hammond, G. W. Stuart, and A. Ayele (2011), Mapping the evolving strain field in the Afar Triple Junction using crustal anisotropy, *Nat. Commun.*, *2*, 285, doi:10.1038/ncomms1287.
Kendall, J. (1994), Teleseismic arrivals at a mid-ocean ridge: Effects of mantle melt and anisotropy, *Geophys. Res. Lett.*, *21*, 301–304.
Kind, R., J. Ni, W. Zhao, J. Wu, X. Yuan, L. Zhao, E. Sandvol, C. Reese, J. Nabelek, and T. Hearn (1996), Evidence from earthquake data for a partially molten crustal layer in southern Tibet, *Science*, *274*(5293), 1692–1694.
Langston, C. A. (1979), Structure under Mount Rainier, Washington, inferred from teleseismic body waves, *J. Geophys. Res.*, *84*, 4749–4762.
Laske, G., G. Masters, Z. Ma, and M. Pasyanos (2013), Update on CRUST1.0—A 1-degree Global Model of Earth's Crust, in *EGU General Assembly Conference Abstracts, Geophys. Res. Abstr.*, vol. *15*, pp. 1658, European Geophysical Union, Vienna, Austria.
Levin, V., and J. Park (1997a), Crustal anisotropy in the Ural Mountains foredeep from teleseismic receiver functions, *Geophys. Res. Lett.*, *24*, 1283–1286.
Levin, V., and J. Park (1997b), P-SH conversions in a flat-layered medium with anisotropy of arbitrary orientation, *Geophys. J. Int.*, *131*, 253–266.
Levin, V., and J. Park (2002), Crust and upper mantle of Kamchatka from teleseismic receiver functions, *Tectonophysics*, *358*, 233–265.
Levin, V., S. Roecker, P. Graham, and A. Hosseini (2008), Seismic anisotropy indicators in Western Tibet: Shear wave splitting and receiver function analysis, *Tectonophysics*, *462*(1–4), 99–108.
Ligorria, J. P., and C. J. Ammon (1999), Iterative deconvolution and receiver-function estimation, *Bull. Seismol. Soc. Am.*, *89*, 1395–1400.
Liu, H., and F. Niu (2012), Estimating crustal seismic anisotropy with a joint analysis of radial and transverse receiver function data, *Geophys. J. Int.*, *188*(1), 144–164.
Maclennan, J., D. McKenzie, K. Gronvöld, and L. Slater (2001), Crustal accretion under northern Iceland, *Earth Planet. Sci. Lett.*, *191*(3), 295–310.
McNamara, D. E., and T. J. Owens (1993), Azimuthal shear wave velocity anisotropy in the Basin and Range province using Moho Ps converted phases, *J. Geophys. Res.*, *98*, 12,003–12,017.
Mohsen, A., R. Hofstetter, G. Bock, R. Kind, M. Weber, K. Wylegalla, G. Rumpker, and the DESERT Group (2005), A receiver function study across the Dead Sea Transform, *Geophys. J. Int.*, *160*(3), 948–960.
Montagner, J. (1998), Where can seismic anisotropy be detected in the Earth's mantle? In boundary layers. . ., *Pure Appl. Geophys.*, *151*, 223–256.
Mooney, W. D., and T. M. Brocher (1987), Coincident seismic reflection/refraction studies of the continental lithosphere: A global review, *Rev. Geophys.*, *25*, 723–742.
Nagaya, M., H. Oda, H. Akazawa, and M. Ishise (2008), Receiver functions of seismic waves in layered anisotropic media: Application to the estimate of seismic anisotropy, *Bull. Seismol. Soc. Am.*, *98*(6), 2990–3006.
Nagaya, M., H. Oda, and T. Kamimoto (2011), Regional variation in shear-wave polarization anisotropy of the crust in southwest Japan as estimated by splitting analysis of Ps-converted waves on receiver functions, *Phys. Earth Planet. Inter.*, *187*(1–2), 56–65.
Obrebski, M., S. Kiselev, L. Vinnik, and J. Montagner (2010), Anisotropic stratification beneath Africa from joint inversion of SKS and P receiver functions, *J. Geophys. Res.*, *115*, B09313, doi:10.1029/2009JB006923.
Oldenburg, D. W. (1981), A comprehensive solution to the linear deconvolution problem, *Geophys. J. R. Astron. Soc.*, *65*, 331–357.
Owens, T. J., G. Zandt, and S. R. Taylor (1984), Seismic evidence for an ancient rift beneath the Cumberland Plateau, Tennessee: A detailed analysis of broadband teleseismic P waveforms, *J. Geophys. Res.*, *89*, 7783–7795.
Ozacar, A. A., and G. Zandt (2009), Crustal structure and seismic anisotropy near the San Andreas Fault at Parkfield, California, *Geophys. J. Int.*, *178*(2), 1098–1104.
Ozacar, A. A., G. Zandt, H. Gilbert, and S. L. Beck (2010), Seismic images of crustal variations beneath the East Anatolian Plateau (Turkey) from teleseismic receiver functions, in *Sedimentary Basin Tectonics From the Black Sea and Caucasus to the Arabian Platform*, vol. *340*, edited by M. Sosson, et al., pp. 485–496, Geol. Soc. Spec. Publ., London, U. K.
Park, J., and V. Levin (2000), Receiver functions from multiple-taper spectral correlation estimates, *Bull. Seismol. Soc. Am.*, *90*(6), 1507–1520.
Savage, M. K. (1998), Lower crustal anisotropy or dipping boundaries? Effects on receiver functions and a case study in New Zealand, *J. Geophys. Res.*, *103*, 15,069–15,087.
Schulte-Pelkum, V., G. Monsalve, A. Sheehan, M. R. Pandey, S. Sapkota, R. Bilham, and F. Wu (2005), Imaging the Indian subcontinent beneath the Himalaya, *Nature*, *435*(7046), 1222–1225.
Silver, P. G. (1996), Seismic anisotropy beneath the continents: Probing the depths of geology, *Annu. Rev. Earth Planet. Sci.*, *24*, 385–432.
Silver, P. G., and W. W. J. Chan (1991), Shear-wave splitting and subcontinental mantle deformation, *J. Geophys. Res.*, *96*, 16,429–16,454.
Stuart, G. W., I. D. Bastow, and C. J. Ebinger (2006), Crustal structure of the northern Main Ethiopian Rift from receiver function studies, in *The Afar Volcanic Province Within the East African Rift System*, vol. *259*, edited by G. Yirgu, C. J. Ebinger, and P. K. H. Maguire, pp. 55–72, Geol. Soc. Spec. Publ., London, U. K.
Tandon, G. P., and G. J. Weng (1984), The effect of aspect ratio of inclusions on the elastic properties of unidirectionally aligned composites, *Polym. Composites*, *5*, 327–333.
Thomsen, L. (1986), Weak elastic anisotropy, *Geophysics*, *51*(10), 1954–1966.
Walker, A. M., and J. Wookey (2012), MSAT—A new toolkit for the analysis of elastic and seismic anisotropy, *Comput. Geosci.*, *49*, 81–90.
Wookey, J. (2012), Direct probabilistic inversion of shear-wave data for seismic anisotropy, *Geophys. J. Int.*, *189*, 1025–1037, doi:10.1111/j.1365-246X.2012.05405.x.
Wright, T. J., et al. (2012), Geophysical constraints on the dynamics of spreading centres from rifting episodes on land, *Nat. Geosci.*, *5*(4), 242–250.
Xu, L., S. Rondenay, and R. D. van der Hilst (2007), Structure of the crust beneath the southeastern Tibetan plateau from teleseismic receiver functions, *Phys. Earth Planet. Inter.*, *165*(3), 176–193.
Xu, X., Z. Ding, D. Shi, and X. Li (2013), Receiver function analysis of crustal structure beneath the eastern Tibetan plateau, *J. Asian Earth Sci.*, *73*, 121–127.
Yang, H., J. Hu, Y. Hu, Y. Duan, and G. Li (2013), Crustal structure in the Tengchong volcanic area and position of the magma chambers, *J. Asian Earth Sci.*, *73*, 48–56.
Zandt, G., and C. J. Ammon (1995), Continental crust composition constrained by measurements of crustal Poisson's ratio, *Nature*, *374*, 152–154.
Zhu, L., and H. Kanamori (2000), Moho depth variation in southern California from teleseismic receiver functions, *J. Geophys. Res.*, *105*, 2969–2980.